Cobalt/Manganese Oxides as Theragnosis Nanoplatforms With Magnetic Resonance/Near-Infrared Imaging for Efficient Photothermal Therapy of Tumors

Jichun Liu[1†], Genfa Wu[1†], Zhiyong Tang[1], Qi Sun[1], Jianxin Wu[2]* and Renfa Lv[1]*

[1] Department of Orthopedics, 908th Hospital of the PLA, Yingtan, China, [2] Department of Orthopedics, Shanghai Changhai Hospital, Shanghai, China

The combination of near-infrared (NIR) response and imaging response is a hot research area in which the functions of nanomaterials are maximized. However, the types of such materials reported so far present problems such as requiring complex synthesis. In this study, hydrophilic, porous, and hollow cobalt/manganese oxide (CMO) nanocrystals (NCs) were successfully prepared via a facile and green hydrothermal route. The CMO NCs show strong near-infrared (NIR) absorption, which results from their defect structure due to the coexistence of Co^{2+} and Co^{3+} in the as-prepared CMO NCs. Thus, the CMO NCs exhibit excellent photothermal performance, showing photothermal efficiency of up to 43.2%. In addition, the CMO NCs possess good magnetic resonance (MR) imaging performance, with longitudinal relaxivity (r_1) of up to 3.48 mM^{-1} s^{-1}. Finally, for the first time, we prove that the CMO nanocrystals are a promising photothermal agent. Our work provides insights into the application of Mn-based control agents and photothermal agents for photothermal theragnosis therapy.

Keywords: cobalt/manganese oxides, photothermal agents, near-infrared absorption, photothermal theragnosis therapy, magnetic resonance imaging

INTRODUCTION

Photothermal therapy (PTT), a promising approach to cancer treatment (Li et al., 2010, 2013; Hessel et al., 2011; Tian et al., 2011), has attracted widespread attention recently because of its superior advantages over traditional treatments such as chemotherapy, surgery, and radiation therapy. The key to the success of photothermal therapy is the development of photothermal agents. Currently, various kinds of photothermal agents are being been explored, including metal nanoparticles (Lee et al., 2019; Zhang D. et al., 2019), carbon-based nanomaterials (Wang et al., 2016; Sobhani et al., 2017), semiconductors (Mou et al., 2015; Zhang X. et al., 2019), and organic compounds (Zha et al., 2013). However, PTT alone is not enough, because contemporary medical diagnosis and treatment require accurate and detailed information on the cancers (i.e., their shape, location, and size). Thus, contrast agents must be introduced. Therefore, nanomaterials that couple near-infrared absorption and imaging properties are much more fit for treating cancers (Hahn et al., 2010; Lee et al., 2012). However, multifunctional nano-biomaterials are mainly composite materials

[for example, MnSe@Bi_2Se_3 (Song et al., 2015) and Fe_3O_4 @Cu_{2-x}S nanoparticles (Tian et al., 2013)], which usually have a rather complicated and cumbersome preparation procedure, resulting in low productivity and heterogeneity. Therefore, a single material that combines NIR and imaging properties [such as Cu_3BiS_3 (Liu et al., 2016), Cu-Fe-S (Zhao et al., 2016), and WO_{3-x} (Chen et al., 2013)] is preferable for photothermal theragnosis therapy, and great efforts have been made in this respect.

Manganese-based oxide nanomaterials (Chen et al., 2014; Song et al., 2015) have been proved to be a promising substitute for gadolinium nanomaterials (Jao et al., 2010; Chen et al., 2014) and have been clinically used as imaging contrast agents for MR imaging. Moreover, manganese is an essential element of the human body. However, manganese-based nanomaterials that have been previously reported (such as MnSe and MnO_2) have very poor absorption properties in the NIR range and thus cannot be used as photothermal agents (Song et al., 2016). One possible solution is to develop a manganese-based nanomaterial with a porous structure in which the photothermal efficiency can be improved (Dong et al., 2013).

In this work, we report the application of hydrophilic porous and hollow cobalt/manganese oxide (CMO) nanocrystals (NCs) as photothermal and T_1-MR imaging control agents. This work, as far as we know, is the first report in which CMO NCs are used as photothermal agents, a functionality that results from their unique porous and hollow structure. These NCs also possess impressive T_1-MR imaging performance, with the longitudinal relaxivity (r_1) up to 3.48 mM^{-1} s^{-1}. Due to the coexistence of Co^{2+} and Co^{3+} in the as-prepared CMO NCs, the resulting NCs exhibit very intense NIR absorption due to electron transitions between Co^{2+} and Co^{3+}. Therefore, the hydrophilic CMO NCs can be used as an excellent NIR-induced photothermal agent. Furthermore, the hydrophilic CMO NCs show excellent biocompatibility.

RESULTS AND DISCUSSION

Synthesis and Characterization

Hydrophilic porous and hollow CMO NCs were synthesized via a simple hydrothermal method by the reaction of $Co(NO_3)_2$ with $KMnO_4$ in a DMF solution at 120°C for 24 h. During preparation, polyvinylpyrrolidone (PVP) was added into the reaction as a surface ligand to improve their biocompatibility, and this coating was determined by FTIR (**Figure S1**). Thus, the CMO NCs are hydrophilic and can be used as photothermal agents without any further modification. Scanning electron microscope (SEM, **Figure 1A**) and transmission electron microscopy (TEM, **Figure 1B**) images demonstrate that the as-prepared products were porous and hollow. The size of the NCs was found to be 80 nm based on the TEM and SEM images (**Figure S2**). Furthermore, the size of the NCs in buffer solution (such as PBS) as determined by dynamic light scattering (DLS) shows almost no change over time, confirming that they have excellent dispersion (**Figure S3**). X-ray photoelectron spectroscopy (XPS, **Figure S4**) revealed the composition and elemental state of the as-prepared products. It showed that the products mainly contain

the elements O, Mn, and Co, with no other impurities. We also analyzed the valency state of Mn and Co in the CMO NCs. **Figure 1C** shows the Mn 2p spectrum for the CMO NCs. The binding energy of Mn 2p$_{1/2}$ (653.7 eV) and Mn 2p$_{3/2}$ (641.6 eV) can be assigned to Mn (IV) coordinated to Mn in CMO (Wang et al., 2003). Also, the binding energy of Co (**Figure 1D**) in the peaks at 779.9 and 795.0 eV, as well as two shakeup satellites demonstrated that there was a mixed cobalt oxidation state, i.e., Co^{2+} and Co^{3+} (Tang et al., 2016), indicating a defect structure in the CMO NCs. The CMO NCs obtained were further characterized by X-ray powder diffraction (XRD) (**Figure S5**). It was seen that the crystal phase of the nanocrystals consisted of Co_3O_4 and MnO_2, confirming the formation of CMO. According to the above results, it can be concluded that porous and hollow CMO NCs were successfully formed.

Photothermal Performance

Photothermal agents with intense NIR absorption are necessary to realize photothermal therapy. The general wavelengths of NIR laser sources that emit photothermal agents include 808, 915, 980, and 1064 nm. As shown in **Figure 2A**, the as-prepared MCO NCs show strong absorption from 700 to 1,000 nm due to the defect structure resulting from the coexistence of Co^{2+} and Co^{3+} in as-prepared CMO NCs. By measuring the CMO NC concentration via inductively-coupled plasma atomic-emission spectroscopy (ICP-AES), the excitation coefficient of CMO NCs was determined to be 12.8 Lg^{-1}cm^{-1}. This value is higher than those of CuS and Au nanostructures (Tian et al., 2011; Zhang D. et al., 2019). Thus, the CMO NCs may possess good photothermal performance. The general wavelengths of NIR laser sources that emit photothermal agents include 808, 915, 980, and 1,064 nm. The NIR absorption intensity at 808 nm of the as-prepared nanocrystals is higher than those at other general wavelengths of NIR laser sources, which leads to higher photothermal conversion efficiency. Thus, 808 nm lasers were chosen to evaluate the photothermal performance of CMO NCs. Various concentrations (i.e., 0, 25, 50, and 100 ppm) of CMO NCs were exposed to an 808 nm laser (0.3 W cm^{-2}) to evaluate their photothermal effect. As expected, the CMO NCs showed good photothermal conversion performance, with a concentration-dependent photothermal effect (**Figure 2B**).

The NIR-driven photothermal conversion efficiency of the CMO NCs (50 ppm) was also measured by a modified method similar to that reported by Roper et al. (2007). An aqueous dispersion of CMO NCs was continuously exposed to an 808 nm laser with a power of 0.189 W for 300 s. When the temperature of the system reached a steady state, the 808 nm laser was shut off. The temperature change during cooling was monitored to confirm the rate of heat transfer of the system (**Figure 2C**). Based on Roper's work, the photothermal conversion efficiency (Roper et al., 2007), η_T, was calculated by the following Equation (1):

$$\eta_T = \frac{hA(T_{max} - T_{amb}) - Q_0}{I(1 - 10^{-A_\lambda})} \quad (1)$$

where A is the surface area of the container, h is the heat transfer coefficient, T_{amb} is the temperature of the ambient surroundings,
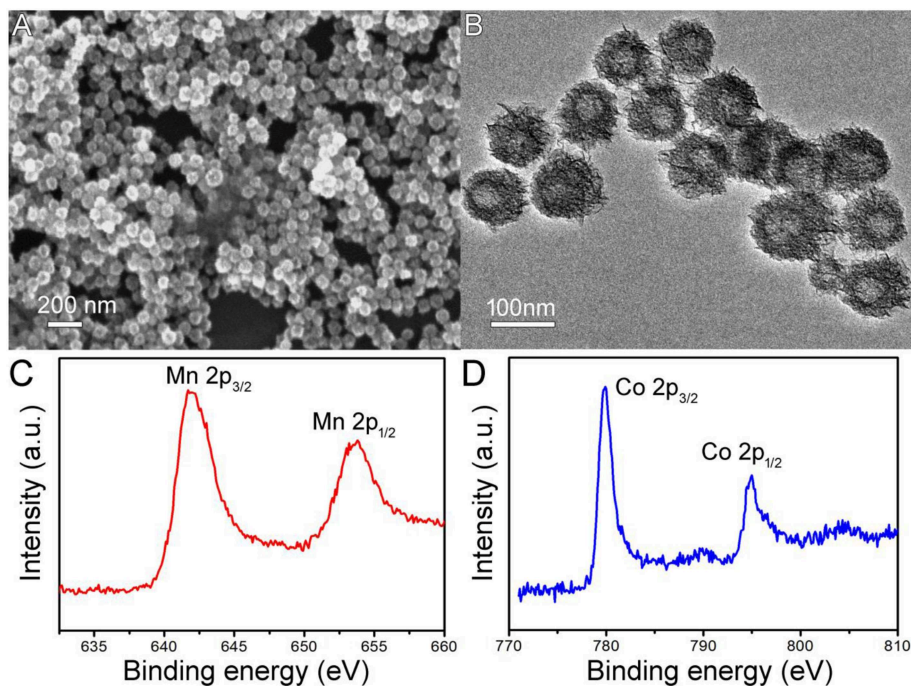
FIGURE 1 | (A) SEM image and (B) TEM image of the as-prepared CMO nanocrystals. XPS spectra of (C) Mn 2p and (D) Co 2p.
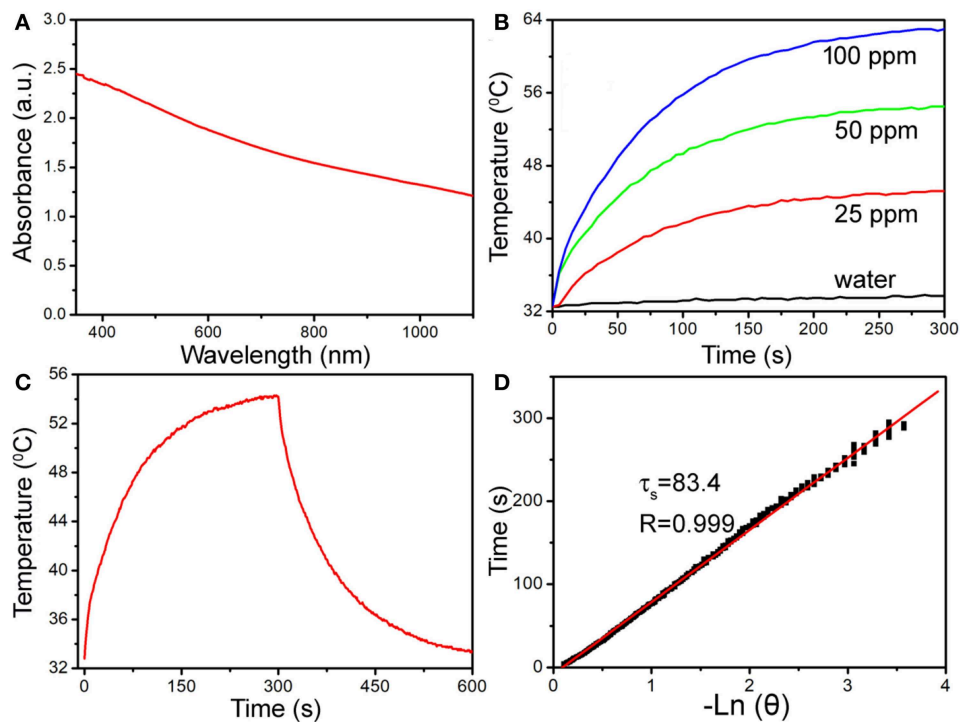

FIGURE 2 | (A) UV-vis-NIR absorbance spectrum of CMO NCs dispersed in water. (B) Temperature change of CMO NCs in water at various Mn^{2+} concentrations (i.e., 0, 25, 50, and 100 ppm) as a function of irradiation time. (C) Photothermal effect of CMO NCs (50 ppm). (D) Time constant of CMO NCs from the system. The laser is an 808 nm laser with a power of 189 mW.

T_{max} is the maximum system temperature, and $(T_{max} - T_{amb})$ was 21.4°C according to **Figure 2C**. Q_0 is the rate of heat input (mW), A_λ is the absorbance intensity (1.53509) at 808 nm, and I is the laser power used (mW, 189 mW). The value of hA can be obtained from **Figure 2D** and can be derived using the following Equation (2):

$$\tau_s = \frac{m_D C_D}{hA} \qquad (2)$$

where m_D and C_D are the mass of water (0.1 g) and heat capacity (4.2 J g^{-1}) of water, respectively, and τ_s is the time constant. Q_0 was tested to be 27.7 mW. Based on the data recorded, the NIR-driven photothermal conversion efficiency (η_T) of the CMO NCs was calculated to be 43.2%, which is high enough for photothermal therapy of cancers.

In vitro Photothermal Therapy

The excellent photothermal performance of MCO NCs indicates that these NCs have great potential to be used as phototherapy agents. Before the realization of photothermal therapy with MCO NCs *in vivo*, their cytotoxicity was measured through a CCK-8 assay with Saos-2 cells. From **Figure S6A**, we can see that these MCO NCs appeared to have very low toxicity. The *in vitro* phototherapy therapy effect of MCO NCs to Saos-2 cells was then studied. After the different treatments indicated in **Figure S6B**, a CCK-8 evaluation was first used to judge the cell mortality rate. The resulted of CCK-8 assay demonstrated that the laser or MCO NCs alone could not kill the cells but that the cell mortality rate for the MCO NCs at 50 ppm combined with 808-nm-laser irradiation was ~95%, indicating a significantly photothermal effect *in vitro*. Moreover, to visualize the *in vitro* phototherapeutic effect of CMO NCs, Saos-2 cells after the indicated treatments were co-stained with propidium iodide (PI) and calcein-AM. The result of live/dead cell staining analysis (**Figure 3**) matched well with those of CCK-8 evaluation, further confirming an efficient *in vitro* photothermal effect.

MR Imaging

In addition to serving as photothermal agents, CMO NCs can also serve as an imaging contrast agent. Phantom imaging and proton T_1 relaxation tests were carried out on CMO NCs at varied Mn concentrations. As shown in **Figure 4A**, the T_1-weighted MR imaging signal intensity was increased with an increase in the concentration of CMO nanocrystals. The longitudinal relaxivity (r_1) value of the CMO NCs was calculated to be 3.48 mM^{-1} s^{-1}, indicating that they are an efficient MRI contrast agent (**Figure 4B**).

We then evaluated the T_1-weighted MRI signal of CMO NCs in animal experiments. From **Figure 4C**, we can see that the signal in tumor sites increased over time after intravenous injection of a PBS solution of CMO NCs due to the enhanced permeability and retention (EPR) effect. Therefore, CMO NCs can serve as an efficient T_1-weighted MR imaging contrast agent.

In vivo Photothermal Therapy

We then evaluated photothermal therapy of cancers *in vivo*. First, the mice were divided into four groups, referred to as (a) CMO NC injection + 808-nm laser irradiation (Group 1, Treatment), (b) PBS + 808 nm laser irradiation (Group 2, Laser), (c) saline injection (Group 3, Saline), and (d) CMO NC injection (Group 4, NCs). An infrared thermal camera was applied to measure the temperature change at tumor sites. Due to the excellent photothermal effect of CMO NCs, infrared thermal images with obvious contrast were achieved (inset in **Figure 5A**). As we can see in **Figure 5A**, the temperatures of the tumor surface could increase dramatically from ~31 to 62°C due to the excellent photothermal effect of CMO NCs.

After the indicated treatment, the tumor sizes and body weights in each group were recorded every 2 days. As shown in **Figure 5B**, the tumors of mice in the treatment group disappeared, and no reoccurrence was observed (**Figure 5B**, **Figure S7**). In marked contrast, the tumors gradually increased in the three control groups and did not differ between those groups. In addition, there was no obvious difference in body weight among the four groups of mice (**Figure 5C**), indicating that the given conditions did not produce obvious toxic effects.

Hematoxylin and eosin (H&E) staining analysis of tumor slices from each group was also conducted to evaluate the photothermal therapy effect. The morphology and size of tumor cells in the three control groups (Groups 2–4) showed little change, while the tumor cells in the experimental group (Group 1) showed obvious necrosis (**Figure 5D**). These results are matched well with the tumor growth data. Therefore, CMO NCs can be used as efficient photothermal theragnosis agents with the irradiation of an 808-nm laser.

Finally, the *in vivo* long-term toxicity of the as-prepared CMO NCs was evaluated by histological examination of major organs to observe the shape and the size of cells after intravenous injection of CMO NCs at a dosage of 15 mg/kg. The organs included the lung, heart, spleen, liver, and kidney. As shown in **Figure 6**, there is no tissue damage or adverse effect compared with those of the control groups. This suggests that these CMO NCs, under the given conditions, are not obviously toxic.

CONCLUSION

In conclusion, CMO NCs with a porous and hollow structure, as a new imaging-guided photothermal therapy agent, have been successfully prepared by a simple hydrothermal route. The as-prepared CMO NCs have good dispersion and show intense NIR absorption owning to their defect structure, and thus exhibit excellent photothermal conversion performance. They are also effective for MR imaging *in vivo*. Furthermore, the *in vitro* and *in vivo* toxicity results indicate their excellent biocompatibility. With the exposure to NIR light and an external magnetic field, the CMO NCs can be used as theragnosis nanoplatforms with MR/NIR imaging for efficient photothermal theragnosis therapy.

EXPERIMENTAL SECTIONS

Synthesis of Hydrophilic CMO NCs

First, 1 mmol $Co(NO_3)_2$ and 0.25 mmol $KMnO_4$ were consecutively dissolved in 40 mL N, N-dimethylformamide (DMF). Next, 500 mg of poly (vinyl pyrrolidone) (PVP) was added. The reaction was then kept at 120°C for 24 h in a
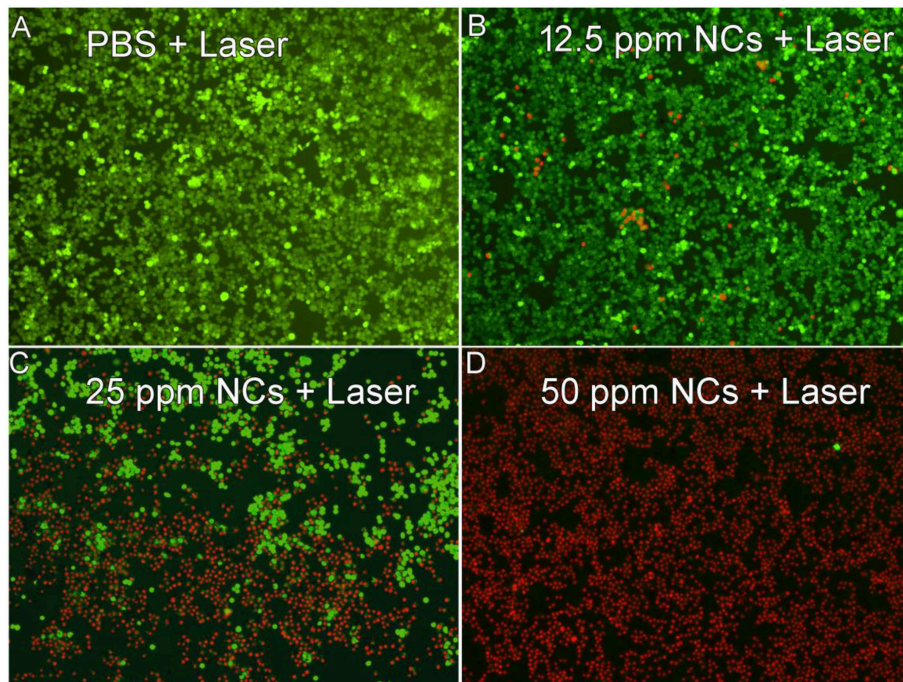
FIGURE 3 | Live/dead cell staining analysis after incubation with CMO NCs at indicated concentrations: **(A)** PBS, **(B)** 12.5 ppm, **(C)** 25 ppm, **(D)** 50 ppm, and then under the exposure of an 808 nm (0.3 W/cm^{-2}) for 5 min. Magnification: 100 times.
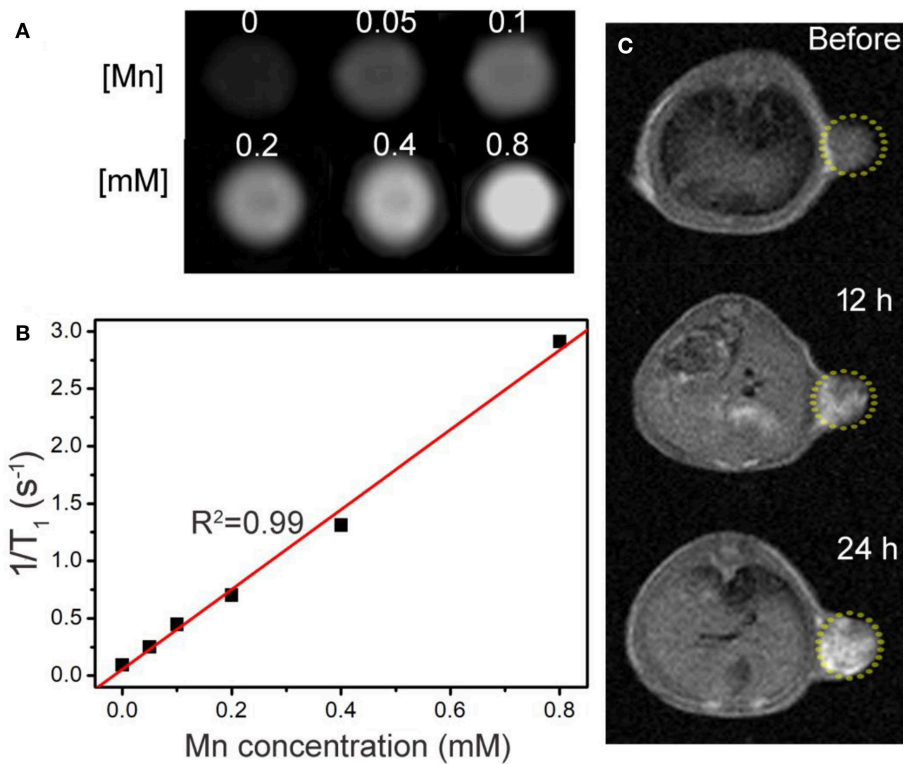

FIGURE 4 | (A) Phantom images of the CMO NCs. **(B)** Proton T_1 relaxation measurements at varied Mn concentrations **(C)** T_1-weighted MR imaging *in vivo* of a tumor-bearing mouse before and after intravenous injection of a solution of CMO NCs. The position of the tumor is marked by yellow dotted circles.
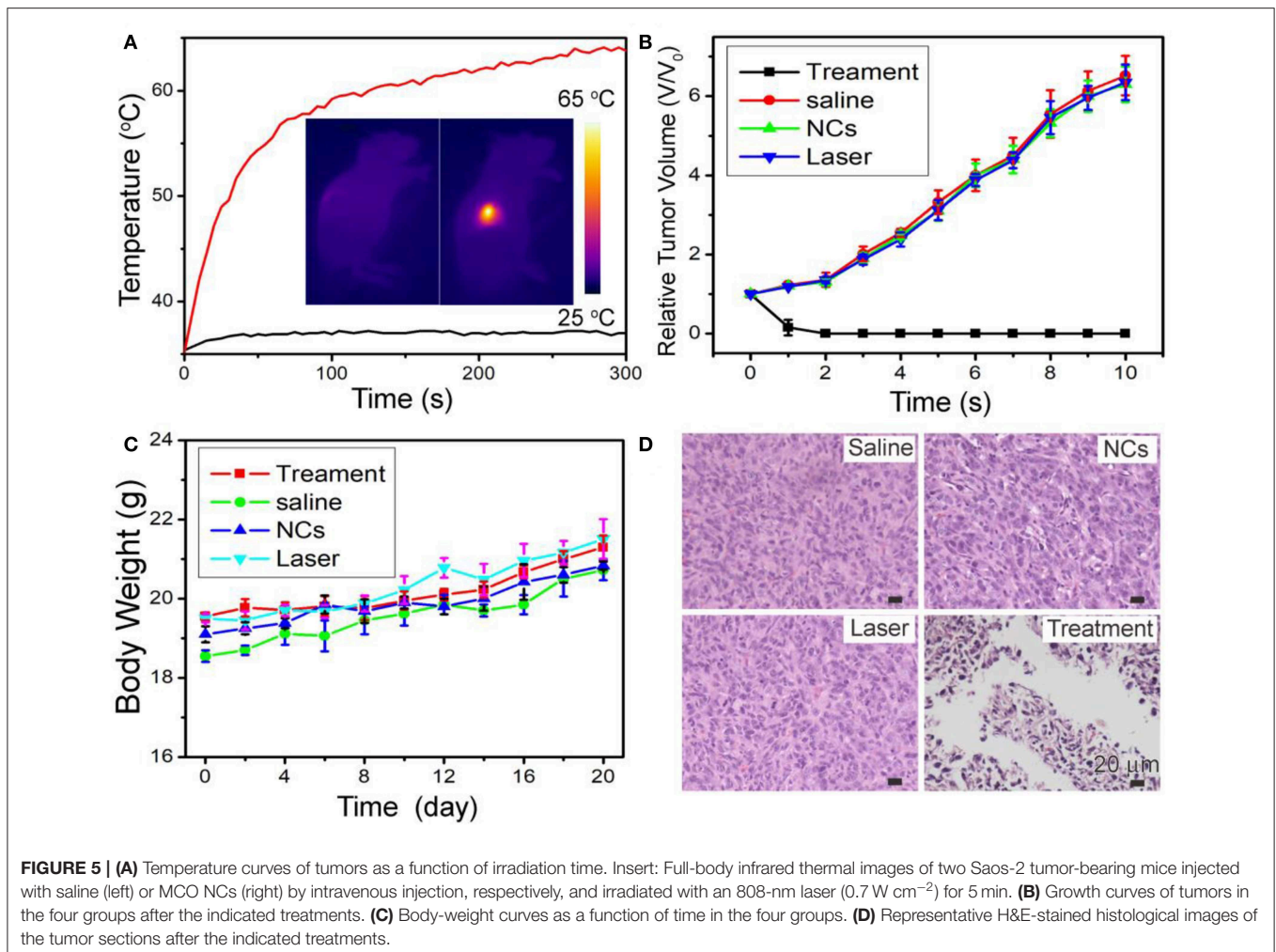
FIGURE 5 | (A) Temperature curves of tumors as a function of irradiation time. Insert: Full-body infrared thermal images of two Saos-2 tumor-bearing mice injected with saline (left) or MCO NCs (right) by intravenous injection, respectively, and irradiated with an 808-nm laser (0.7 W cm^{-2}) for 5 min. **(B)** Growth curves of tumors in the four groups after the indicated treatments. **(C)** Body-weight curves as a function of time in the four groups. **(D)** Representative H&E-stained histological images of the tumor sections after the indicated treatments.
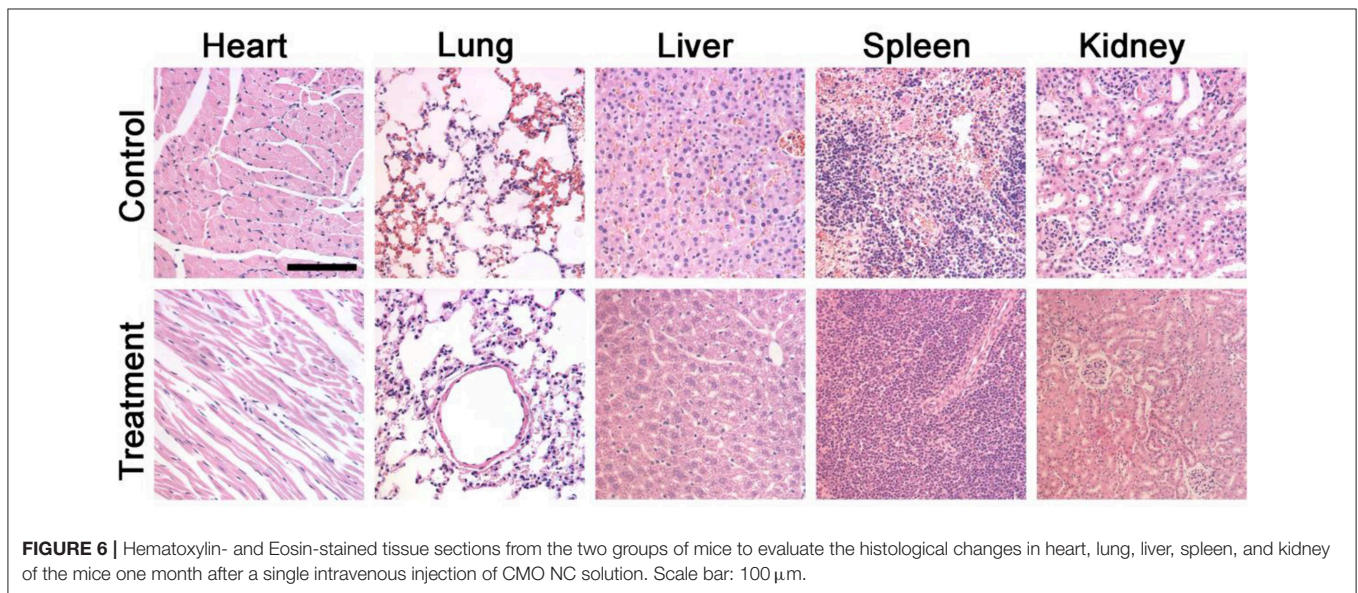

FIGURE 6 | Hematoxylin- and Eosin-stained tissue sections from the two groups of mice to evaluate the histological changes in heart, lung, liver, spleen, and kidney of the mice one month after a single intravenous injection of CMO NC solution. Scale bar: 100 μm.

stainless steel autoclave. The products were collected through centrifugation and were finally washed with ethanol and deionized water three times.

Characterization

The morphology and the size of the NCs was determined by TEM (JEM-2100F, JEOL, Japan). UV-Vis-NIR absorbance spectra were obtained with a UV-Visible-NIR spectrophotometer (UV-1902PC, Phenix) at room temperature. The crystal phase of CMO NCs was measured by XRD (Rigaku D/Max-2550 V, Geigerflex). The oxidation state of the CMO NCs was measured through X-ray photoelectron spectra (XPS, ESCA-Lab 250Xi). The concentration of Mn ions released from CMO NCs was tested by ICP-AES (Leeman Laboratories Prodigy).

Measurement of the Photothermal Effect of CMO NCs

For the evaluation of the photothermal performance of CMO NCs, 100 μL of CMO NCs dispersed in deionized water at various concentrations was exposed to irradiation from an 808 nm laser. The temperature change was recorded by a thermal imaging camera.

In vitro Cellular Experiment of CMO NCs

Saos-2 cells were used as the model of cancer cells to assess the biocytotoxicity of the CMO NCs. Saos-2 cells were cultured in Dulbecco's modified Eagle's medium (DMEM) combined with 5% CO_2 at 37°C prior to use. For cytotoxicity evaluation *in vitro*, Saos-2 cells (1×10^4 cells per well) were seeded in 96-well plates. After cultivation for 24 h, the upper layer of the DMEM medium was removed through a straw and was washed several times by PBS. CMO NCs dispersed in DMEM at varied concentrations were then added into the wells. After 24 h, a CCK8 (Dojindo Laboratories, Kumamoto) assay was used to measure cell viability. For photothermal therapy of Saos-2 cells *in vitro*, the cell suspension was dispensed in 200 μL centrifuge tubes (1×10^5 cells every tube) and incubated with CMO NCs. These Saos-2 cells were then irradiated with an 808 nm laser (0.3 W cm^{-2}) for 5 min. After that, the Saos-2 cells were co-stained with propidium iodide (PI) and calcein-AM. The live/dead fluorescence images were taken with a fluorescence microscope (Leica DMi8). All of the experiments were carried out four times.

MR Imaging

The dispersions of CMO NCs with varied Mn concentrations (0–0.8 mM) were scanned at room temperature via an animal MR imaging scanner, using a 0.5 T MRI scanner at room temperature. All animal procedures were agreed on with the institutional animal use and care committee at Shanghai Changhai Hospital

and were carried out ethically and humanely. For MR imaging *in vivo*, mice were scanned with the same MR scanner with the same parameters after intravenous injection with the CMO NC dispersion (100 μL, 15 mg/kg).

In vivo Photothermal Therapy

The nude mice were subcutaneously injected with Saos-2 cells (5×10^6 per mouse) into the right thigh to establish the tumor models. After the tumor volumes reached about ∼100 mm³, Saos-2 tumor-bearing mice were then divided into four groups (six mice in each group). CMO NC solution (100 μL, 100 ppm) or PBS solution were intravenously injected in the tumor sites of the nude mice. The nude mice without or with the CMO NC injection were exposed to an 808 nm laser (0.7 W cm^{-2}) for 5 min. The temperature of the tumor surface was monitored with an infrared thermal camera. The tumor size and body weight were measured every two days after treatment. Relative tumor volumes were calculated as V/V_0, where V_0 was the initial tumor volume before the therapy.

Histological Examination

For histological examination of the tumors, one mouse in each group was killed under anesthesia after the indicated treatment. The tumors were then harvested, sectioned into 4 μm slices using a conventional microtome, and finally stained with H&E. The slices were examined by microscope.

DATA AVAILABILITY STATEMENT

All datasets generated for this study are included in the article/**Supplementary Material**.

ETHICS STATEMENT

The animal study was reviewed and approved by the ethics committee of Shanghai Changhai hospital.

AUTHOR CONTRIBUTIONS

JW and RL designed the project. JL, GW, ZT, and QS carried out the experiment and performed the experimental data analysis. JL and GW wrote the paper. All of the authors contributed to discussion of the results.

SUPPLEMENTARY MATERIAL

The Supplementary Material for this article can be found online at: https://www.frontiersin.org/articles/10.3389/fmats.2019.00286/full#supplementary-material

REFERENCES

Chen, Y., Ye, D. L., Wu, M. Y., Chen, H. R., Zhang, L. L., Shi, J. L., et al. (2014). Break-up of two-dimensional MnO_2 nanosheets promotes ultrasensitive pH-triggered theranostics of cancer. *Adv. Mater.* 26, 7019–7026. doi: 10.1002/adma.201402572

Chen, Z., Wang, Q., Wang, H., Zhang, L., Song, G., Song, L., et al. (2013). Ultrathin PEGylated W18O49 nanowires as a new 980 nm-laser-driven photothermal agent for efficient ablation of cancer cells *in vivo*. *Adv. Mater.* 25, 2095–2100. doi: 10.1002/adma.201204616

Dong, K., Liu, Z., Li, Z., Ren, J., and Qu, X. (2013). Hydrophobic anticancer drug delivery by a 980 nm laser-driven photothermal vehicle for efficient

synergistic therapy of cancer cells *in vivo*. *Adv. Mater.* 25, 4452–4458. doi: 10.1002/adma.201301232

Hahn, M. A., Singh, A. K., Sharma, P., Brown, S. C., and Moudgil, B. M. (2010). Nanoparticles as contrast agents for *in-vivo* bioimaging: current status and future perspectives. *Anal. Bioanal. Chem.* 399, 3–27. doi: 10.1007/s00216-010-4207-5

Hessel, C. M., Pattani, V. P., Rasch, M., Panthani, M. G., Koo, B., Tunnell, J. W., et al. (2011). Copper selenide nanocrystals for photothermal therapy. *Nano Lett.* 11, 2560–2566. doi: 10.1021/nl201400z

Jao, S. Y., Yang, B. Y., Weng, H. H., Yeh, C. H., and Lee, L. W. (2010). Evaluation of gadolinium-enhanced T1-weighted magnetic resonance imaging in the preoperative assessment of local staging in rectal cancer. *Colorectal Dis.* 12, 1139–1148. doi: 10.1111/j.1463-1318.2009.01959.x

Lee, D.-E., Koo, H., Sun, I.-C., Ryu, J. H., Kim, K., and Kwon, I. C. (2012). Multifunctional nanoparticles for multimodal imaging and theragnosis. *Chem. Soc. Rev.* 41, 2656–2672. doi: 10.1039/C2CS15261D

Lee, S. B., Lee, J. E., Cho, S. J., Chin, J., Kim, S. K., Lee, I. K., et al. (2019). Crushed gold shell nanoparticles labeled with radioactive iodine as a theranostic nanoplatform for macrophage-mediated photothermal therapy. *Nano Micro Lett.* 11:36. doi: 10.1007/s40820-019-0266-0

Li, W., Zamani, R., Rivera Gil, P., Pelaz, B., Ibanez, M., Cadavid, D., et al. (2013). CuTe nanocrystals: shape and size control, plasmonic properties, and use as SERS probes and photothermal agents. *J. Am. Chem. Soc.* 135, 7098–7101. doi: 10.1021/ja401428e

Li, Y., Lu, W., Huang, Q., Huang, M., Li, C., and Chen, W. (2010). Copper sulfide nanoparticles for photothermal ablation of tumor cells. *Nanomedicine* 5, 1161–1171. doi: 10.2217/nnm.10.85

Liu, J., Wang, P., Zhang, X., Wang, L., Wang, D., Gu, Z., et al. (2016). Rapid degradation and high renal clearance of Cu_3BiS_3 nanodots for efficient cancer diagnosis and photothermal therapy *in vivo*. *ACS Nano* 10, 4587–4598. doi: 10.1021/acsnano.6b00745

Mou, J., Liu, C., Li, P., Chen, Y., Xu, H., Wei, C., et al. (2015). $Cu_{2-x}S$ MRI and infrared thermal/photoacoustic multimodal imaging. *Biomaterials* 57, 12–21. doi: 10.1016/j.biomaterials.2015.04.020

Roper, D. K., Ahn, W., and Hoepfner, M. (2007). Microscale heat transfer transduced by surface plasmon resonant gold nanoparticles. *J. Phys. Chem. C* 111, 3636–3641. doi: 10.1021/jp064341w

Sobhani, Z., Behnam, M. A., Emami, F., Dehghanian, A., and Jamhiri, I. (2017). Photothermal therapy of melanoma tumor using multiwalled carbon nanotubes. *Int. J. Nanomed.* 12, 4509–4517. doi: 10.2147/IJN.S134661

Song, G., Liang, C., Gong, H., Li, M., Zheng, X., Cheng, L., et al. (2015). Core-shell $MnSe@Bi_2Se_3$ fabricated via a cation exchange method as novel nanotheranostics for multimodal imaging and synergistic thermoradiotherapy. *Adv. Mater.* 27, 6110–6117. doi: 10.1002/adma.201503006

Song, M. L., Liu, T., Shi, C. R., Zhang, X. Z., and Chen, X. Y. (2016). Bioconjugated manganese dioxide nanoparticles enhance chemotherapy response by priming tumor-associated macrophages toward M1-like phenotype and attenuating tumor hypoxia. *ACS Nano* 10, 633–647. doi: 10.1021/acsnano.5b06779

Tang, J. H., Ge, Y. C., Shen, J. F., and Ye, M. X. (2016). Facile synthesis of $CuCo_2S_4$ as a novel electrode material for ultrahigh supercapacitor performance. *Chem. Commun.* 52, 1509–1512. doi: 10.1039/C5CC09402J

Tian, Q., Hu, J., Zhu, Y., Zou, R., Chen, Z., Yang, S., et al. (2013). Sub-10 nm $Fe_3O_4@Cu_{2-x}S$ core-shell nanoparticles for dual-modal imaging and photothermal therapy. *J. Am. Chem. Soc.* 135, 8571–8577. doi: 10.1021/ja4013497

Tian, Q., Tang, M., Sun, Y., Zou, R., Chen, Z., Zhu, M., et al. (2011). Hydrophilic flower-like CuS superstructures as an efficient 980 nm laser-driven photothermal agent for ablation of cancer cells. *Adv. Mater.* 23, 3542–3547. doi: 10.1002/adma.201101295

Wang, L. Z., Omomo, Y., Sakai, N., Fukuda, K., Nakai, I., Ebina, Y., et al. (2003). Fabrication and characterization of multilayer ultrathin films of exfoliated MnO_2 nanosheets and polycations. *Chem. Mater.* 15, 2873–2878. doi: 10.1021/cm034191r

Wang, S., Shang, L., Li, L., Yu, Y., Chi, C., Wang, K., et al. (2016). Metal-organic-framework-derived mesoporous carbon nanospheres containing porphyrin-like metal centers for conformal phototherapy. *Adv. Mater.* 28, 8379–8387. doi: 10.1002/adma.201602197

Zha, Z., Yue, X., Ren, Q., and Dai, Z. (2013). Uniform polypyrrole nanoparticles with high photothermal conversion efficiency for photothermal ablation of cancer cells. *Adv. Mater.* 25, 777–782. doi: 10.1002/adma.201202211

Zhang, D., Qin, X., Wu, T., Qiao, Q., Song, Q., and Zhang, Z. (2019). Extracellular vesicles based self-grown gold nanopopcorn for combinatorial chemo-photothermal therapy. *Biomaterials* 197, 220–228. doi: 10.1016/j.biomaterials.2019.01.024

Zhang, X., Liu, J. C., Yang, X. R., He, G. J., Li, B., Qin, J. B., et al. (2019). $CuCo_2S_4$ nanocrystals as a nanoplatform for photothermal therapy of arterial inflammation. *Nanoscale* 11, 9733–9742. doi: 10.1039/C9NR00772E

Zhao, Q., Yi, X., Li, M., Zhong, X., Shi, Q., and Yang, K. (2016). High near-infrared absorbing Cu_5FeS_4 nanoparticles for dual-modal imaging and photothermal therapy. *Nanoscale* 8, 13368–13376. doi: 10.1039/C6NR04444A